Imaging with unfocused regions of focused ultrasound beams

Roger Zemp[a)]
Department of Biomedical Engineering, Washington University in St. Louis, St. Louis, Missouri 63130

Michael F. Insana
Department of Bioengineering, University of Illinois at Urbana-Champaign, Urbana, Illinois

(Received 7 April 2006; revised 18 December 2006; accepted 19 December 2006)

This article gives an analytical, computational, and experimental treatment of the spatial resolution encoded in unfocused regions of focused ultrasound beams. This topic is important in diagnostic ultrasound since ultrasound array systems are limited to a single transmit focal point per acoustic transmission, hence there is a loss of spatial resolution away from the transmit focus, even with the use of dynamic receive focusing. We demonstrate that the spatial bandwidth of a Gaussian-apodized beam is approximately constant with depth, which means that there is just as much encoded spatial resolution away from the transmit focus as there is in the focal region. We discuss the practical application of this principle, present an algorithm for retrospectively focusing signals from unfocused regions of fixed-focus beams, and provide a quantitative comparison between our methods and dynamic-receive beamforming.
[DOI: 10.1121/1.2434247]

PACS number(s): 43.60.Fg [TDM] Pages: 1–XXXX

I. INTRODUCTION

Current ultrasound arrays systems typically transmit acoustic pulses at a fixed focal depth, then dynamically adjust element phase delays so that the receive focus is steered along the receive scan line. Because current arrays systems do not have the ability to dynamically focus on transmission, spatial resolution degrades away from the transmit focus. In this article we discuss the acoustics of unfocused beams in the context of ultrasonic imaging. The framework provides fundamental insights and offers practical applications.

Originally, this work was motivated by a recent detection performance theory developed by our group.[1,2] A Bayesian ideal observer for the task of detecting low contrast lesions was found to have a log-likelihood test statistic which first whitened data by Wiener spatiotemporal deconvolution, then used the filtered image to make a decision about whether a lesion was present or absent. From this perspective, spatiotemporal Wiener filtering is the strategy of the ideal observer, the observer with maximum possible detection performance given full knowledge of the signal likelihoods. Wiener filtering reduces to matched filtering in low signal-to-noise ratio (SNR) conditions or with significant regularization. Spatiotemporal deconvolution methods have been well studied in the literature.[3–7]

Matched rather than Wiener filtering is discussed in this article for simplicity. Spatiotemporal matched filtering involves time-reversal of the point-spread function followed by convolution with the rf image data. Spatiotemporal matched filtering has been investigated, for example, by Jensen and Gori,[8] who proposed that focusing can be accomplished by spatial matched filtering, however, their experimental data were acquired using a weakly focused mechanically scanned transducer, offering little improvement over standard imaging. They suggested using a more highly focused probe to see an image quality advantage. We use an array transducer with electronic focusing and investigate larger numerical aperture scanning. The time-reversal procedure in matched filtering also lends a connection to time-reversal literature.[9,10]

Freeman *et al.*[11] proposed retrospective dynamic transmit focusing by deconvolving out-of-focus transmit regions with a scan angle-independent but depth-dependent filter. They applied their filter to dynamic-receive beamformed data. This approach was modified by Jeng and Huang[12] to account for depth-dependent SNR. While their work focused on correction of dynamic receive focused data, we concentrate on fixed focused beams. We build on the work of Li and Li,[13] who showed a one-dimensional lateral filter for filtering fixed focus wave fronts to improve point-spread function compactness. They showed that filtering techniques with fixed receive focusing can achieve an image quality similar to that of dynamic receive focusing with filtering, a potential advantage for developing low complexity systems.

A number of authors have developed synthetic aperture approaches to accomplish transmit focusing. Nikolov[14] presented an echo SNR-improving technique for synthetic transmit-receive focusing that used a virtual source "behind" an array. This technique allows a greater subaperture to be used for transmission, thus improving transmitted signal power. Additionally, Passman and Ermert[15] and Frazier and O'Brien[16] use a synthetic aperture method for single element transducers, treating the focal region as a virtual source. Our article contains a dynamic focusing extension of their work adapted for array transducers.

The novel contributions in this article include the following: (1) development of an analytic framework for understanding spatial bandwidth in unfocused regions of focused beams. The theory predicts that the spatial bandwidth is approximately conserved throughout the nearfield, farfield, and

[a)]Electronic mail: rzemp@biomed.wustl.edu

focal zone of a fixed focus transducer. (2) We provide a useful approximation of the spatial bandwidth of a beam when the transmit and receive focii differ. (3) We describe a delay-and-sum algorithm for *dynamically* refocusing signals from unfocused regions of fixed-focus ultrasound beams. Our algorithm is an array-based shift-variant extension of the virtual source-detector synthetic aperture method[15,16] for single element transducers. Some advantages of the technique compared to dynamic receive focusing are discussed. (4) We show that by focusing in the nearfield of a fixed unfocused aperture, the beam can be focused retrospectively as if it were transmitted from a low f-number transducer. One practical motivation behind fixed focusing rather than dynamic-receive focusing is that front-end ultrasound system complexity is greatly reduced when no dynamic beamforming circuit is required. One possible ultrasound array system architecture is discussed that would require simply fixed-delay analog delay lines and a single analog-to-digital converter. Another application is for improving pre- and postfocal-zone image quality in systems using mechanically scanned single element transducers.

II. THEORY

A. Unfocused regions of focused beams

We first concentrate on writing the equations of curved wave fronts from focused transducers. Rather than consider the details of individual elements in an array, we model the array as a continuous aperture with defined focusing and apodization properties. Our goal is to derive expressions for the lateral bandwidth of a transducer at axial depths at and away from the focus.

1. Linear systems model

For a single A-scan line, the spatiotemporal impulse response can be written as a series of temporal convolutions,[17]

$$h(\mathbf{x},t) = -\frac{1}{c^2}\frac{\partial^2}{\partial t^2} \times \left\{ h_y(t) * h_y(t) * v(t) * \frac{\partial h_{\mathrm{Tx}}(\mathbf{x},t)}{\partial t} * h_{\mathrm{Rx}}(\mathbf{x},t) \right\}, \tag{1}$$

where h_y is the electromechanical impulse response of the transducer, $v(t)$ is the excitation voltage, and h_a (where "a" represents the transmit "Tx" or receive "Rx" aperture) is the acoustic impulse response of the transducer given by the Rayleigh integral

$$h_a(\mathbf{x},t) = \frac{1}{2\pi}\int_S dS\,\xi(r)\frac{\delta(t-|\mathbf{r}-\mathbf{x}|/c)}{|\mathbf{r}-\mathbf{x}|}. \tag{2}$$

Here ξ is the transducer apodization function, and the vector $\mathbf{r}$ defines points on the surface of the transducer S.

2. Spatial frequency domain

As we are interested in the spatial and temporal bandwidth characteristics with various focusing configurations, we need to calculate the Fourier magnitude of the point-spread function as a function of $\mathbf{u}$ (the spatial frequency vector conjugate to $\mathbf{x}$) and f (the temporal frequency conjugate to time t). To obtain the two-dimensional Fourier magnitude $|H(u_2,f)|$ of $\mathrm{psf}(x_2,t)=h(x_2,t|x_1,x_3)$ we need the Fourier transform of $\partial h_{Tx}(\mathbf{x},t)/\partial t *_t h_{\mathrm{Rx}}(\mathbf{x},t)$, given as

$$i2\pi f[H_{\mathrm{Tx}}(u_2,f|x_1,x_3) * H_{\mathrm{Rx}}(u_2,f|x_1,x_3)] \tag{3}$$

where f is the temporal frequency, $H_a(u_2,f|x_1,x_3) = \mathcal{F}_{x_2,t}\{h_a(\mathbf{x},f)\}$, and all other quantities are temporal Fourier transforms of the quantities in Eq. (1). The convolution is strictly over spatial frequencies u_2.

3. Fresnel approximation

We begin our computation of $H_a(u_2,f|x_1,x_3)$ for the transmit (or receive) aperture by using the Fresnel approximation[18] to compute

$$h_a(\mathbf{x},f) \cong \frac{e^{ikx_1}}{i\lambda x_1}e^{i(k/2x_1)(x_2^2+x_3^2)}\int dS\,\xi(\mathbf{r})e^{i(k/2x_1)|\mathbf{r}|^2}e^{-i(k/x_1)\mathbf{x}\cdot\mathbf{r}} \tag{4}$$

The Fresnel approximation is applicable for quasiplanar apertures and for paraxial points far from the aperture with respect to the aperture dimensions.

4. Lateral BW of Gaussian apodized fixed focus transducer

In this section we consider Gaussian apodized transducers having identical transmit and receive focus. Without the assumption of Gaussian apodization the analysis is less transparent. Let us consider a separable complex apodization function $\xi(r_2,r_3)=\xi_2(r_2)\xi_3(r_3)$ for quasiplanar transducers, where the azimuthal apodization functions can be considered a product of a real Gaussian apodization and a complex phase term representing focusing:

$$\xi_2(r_2) = e^{-r_2^2/2\sigma_2^2}e^{-jk[\sqrt{F^2+r_2^2}-F]} \tag{5}$$

where F is the focal length. For analytical convenience we do not impose any finite aperture—we simply assume that the Gaussian apodization is not severely truncated, i.e., that the aperture width L is significantly greater than σ_2. Additionally we find it advantageous to assume parabolic focusing by expanding the complex argument of Eq. (5) in a second-order Taylor series expansion in r_2 about 0 so that $\sqrt{F^2+r_2^2}-F \cong r_2^2/(2F)$. With these approximations, Eq. (4) can be integrated by completing the square to become

$$h_a(\mathbf{x},f) \cong \frac{k}{j2\pi x_1}e^{jkx_1}\sqrt{2\pi\sigma_3^2}\sqrt{\frac{\pi}{a_2}}e^{-\Psi x_2^2} \tag{6}$$

where

$$\frac{1}{a_2} = \frac{\dfrac{1}{2\sigma_2^2} - j\dfrac{k}{2}\left(\dfrac{1}{F}-\dfrac{1}{x_1}\right)}{\left(\dfrac{1}{2\sigma_2^2}\right)^2 + \left(\dfrac{k}{2}\right)^2\left(\dfrac{1}{F}-\dfrac{1}{x_1}\right)^2}. \tag{7}$$

Ψ is a complex quantity $\Psi=\Psi_r+j\Psi_i$, with real and imaginary parts given as

$$\Psi_r = \left(\frac{k}{2x_1}\right)^2 \frac{1/2\sigma_2^2}{\left(\frac{1}{2\sigma_2^2}\right)^2 + \left(\frac{k}{2}\right)^2\left(\frac{1}{F}-\frac{1}{x_1}\right)^2} \cong \frac{1}{2\sigma_2^2}\frac{F^2}{(F-x_1)^2} \tag{8}$$

and

$$\Psi_i = \left(\frac{k}{2x_1}\right)^2 \frac{\left(\frac{k}{2}\right)\left(\frac{1}{F}-\frac{1}{x_1}\right)}{\left(\frac{1}{2\sigma_2^2}\right)^2 + \left(\frac{k}{2}\right)^2\left(\frac{1}{F}-\frac{1}{x_1}\right)^2} + \frac{k}{2x_1}$$

$$\cong \left(\frac{k}{2}\right)\left(\frac{1}{x_1-F}\right), \tag{9}$$

respectively. The approximation is true for points x_1 away from the focus when $k|x_1-F| \gg (F/\sigma_2)(x_1/\sigma_2)$. For F-numbers greater than 1 and for distances x_1 within a couple of focal lengths from the origin, this approximation means that the distance from the focus should be more than a few wavelengths.

The real part defines a lateral Gaussian envelope $e^{-\Psi_r x_2^2}$ for h_a, and the imaginary part defines a linear spatial frequency phase modulation $e^{-i(\Psi_i x_2)x_2}$, i.e., a baseband chirp, where Ψ_i determines the linear chirp rate and increases in magnitude as one approaches the focal region. The extent of chirping is regulated by Ψ_r as this determines the spatial extent of the curved wave fronts.

We need to transform our result to the spatial frequency domain to compute the lateral bandwidth:

$$H_a(u_2,f) \propto \mathcal{F}\{e^{-\Psi x_2^2}\} \propto e^{-\Sigma u_2^2} \tag{10}$$

where

$$\mathrm{Re}\{\Sigma\} = \pi^2 \frac{\Psi_r}{\Psi_r^2+\Psi_i^2} \cong \pi^2 \frac{2F^2}{\sigma_2^2 k^2}. \tag{11}$$

The middle term is valid for the full expressions of Ψ_r and Ψ_i. The approximation is valid at the focus when $2\pi(\sigma_2/\lambda)(\sigma_2/F) \gg 1$ (which is practically always the case), and for points x_1 away from the focus when $k|x_1-F| \gg (F/\sigma_2)(x_1/\sigma_2)$. Equation (10) can be substituted into Eq. (3) to find

$$|H(u_2,f|x_1,x_3)| \propto e^{-2\,\mathrm{Re}(\Sigma)u_2^2} \tag{12}$$

which means that the lateral Gaussian BW for all axial locations x_1 (that satisfy the approximations of the model) can be written as

$$\mathrm{BW}_{\mathrm{lat}} = \frac{2}{\sqrt{\mathrm{Re}(\Sigma)}} = \frac{\sigma_2 k}{F}. \tag{13}$$

Note that the result is constant for nearfield, farfield, and focal axial depths and equal to the reciprocal of the expected focal resolution! This is a rather remarkable result which is validated for arrays using FIELD II simulations[19,20] in Sec. III B.

5. Extension of the concept of time-BW product

The product of the time-duration of a coded wave form with its bandwidth is termed the time-bandwidth product (TBP). The TBP is a unitless quantity that is representative of potential information, and is one for typical pulses and greater than one for coded wave forms. It is appropriate to extend the TBP concept to spatial coding. Here we define a quantity which we shall call the lateral space-BW product ($\mathrm{SBP}_{\mathrm{lat}}$) which is given as the product of the lateral spatial extent of the psf times the lateral BW of the psf. For our Gaussian apodized transducer

$$\mathrm{SBP}_{\mathrm{lat}} = \mathrm{BW}_{\mathrm{lat}}\sigma_{\mathrm{lat}} \cong 1 + \left(\frac{k\sigma_2^2|F-x_1|}{F^2}\right)^2. \tag{14}$$

Note that σ_2 is the Gaussian aperture apodization width, whereas σ_{lat} is defined as the -6 dB lateral width of the psf. As might be expected, the $\mathrm{SBP}_{\mathrm{lat}}$ is one at the focus (no wave front curvature thus no lateral coding). It is greater than 1 away from the focus and is greater for distances far from the focus, the expression holding as long as the Fresnel approximation is obeyed.

6. Differing transmit and receive focii

It can be readily shown that the lateral psf bandwidth due to transmit and receive focii F_{Tx} and F_{Rx} is given as

$$\mathrm{BW}_{\mathrm{lat}} = \frac{\sqrt{2}k}{\sqrt{\left(\frac{F_{\mathrm{Tx}}}{\sigma_{\mathrm{Tx}}}\right)^2 + \left(\frac{F_{\mathrm{Rx}}}{\sigma_{\mathrm{Rx}}}\right)^2}}, \tag{15}$$

where σ_{Tx} and σ_{Rx} are the transmit and receive aperture Gaussian apodization parameters, hence $F_{\mathrm{Tx}}/\sigma_{\mathrm{Tx}}$ and $F_{\mathrm{Rx}}/\sigma_{\mathrm{Rx}}$ are the transmit and receive f-numbers, respectively. Again this expression is approximately true even in the pre- and postfocal regions.

B. Time domain

We are interested in

$$\tilde{h}_i(\mathbf{x},t) \equiv \frac{\partial h_a(\mathbf{x},t)}{\partial t} *_t h_a(\mathbf{x},t). \tag{16}$$

To compute this, consider the temporal frequency domain expression

$$\tilde{h}_i(\mathbf{x},f) = jkc \times h_a^2(\mathbf{x},f) \cong -\frac{jkc}{2}\left(\frac{k}{x_1}\right)^2 e^{j2kx_1}\sigma_3^2\frac{1}{a_2}e^{-2\Psi x_2^2}, \tag{17}$$

where σ_3 is the elevational Gaussian apodization parameter. Before taking the inverse temporal Fourier transform of this, note that the real part of Eq. (7) is a Lorenzian function of k, and thus has an inverse temporal Fourier transform of the form $e^{-\alpha|\tau|}$. The imaginary part also looks like a Lorenzian but has an additional factor of jk in the numerator corresponding to a time derivative in the temporal domain.

When the rightmost term in the denominator of Eq. (7) dominates, the approximation of neglecting $(1/2\sigma_2^2)^2$ is useful because the k^2 in the denominator cancels with a k^2 in the numerator of Eq. (17)—simplifying the analysis. This can be written as

$$\tilde{h}_i(\mathbf{x},f) \cong -\frac{\sigma_3^2}{2}\left(\frac{1}{x_1}\right)^2 \frac{1}{\left(\frac{1}{F}-\frac{1}{x_1}\right)^2} \exp -\frac{1}{\sigma_2^2}\frac{F^2}{(F-x_1)^2}x_2^2 \times j2\pi f e^{j2\pi f \tau_F}\left[\frac{1}{\sigma_2^2} - j\frac{2\pi f}{c}\left(\frac{1}{F}-\frac{1}{x_1}\right)\right] \quad (18)$$

where

$$\tau_F = \frac{2x_1}{c} - \frac{1}{x_1 - F}\frac{x_2^2}{c}. \quad (19)$$

Now proceeding with the inverse temporal Fourier transform, we have

$$h_i(\mathbf{x},t) \cong -\frac{\sigma_3^2}{2}\left(\frac{1}{x_1}\right)^2 \frac{1}{\left(\frac{1}{F}-\frac{1}{x_1}\right)^2} \exp -\frac{1}{\sigma_2^2}\frac{F^2}{(F-x_1)^2}x_2^2 \times \left[\frac{1}{\sigma_2^2} - \frac{1}{c}\left(\frac{1}{F}-\frac{1}{x_1}\right)\frac{d}{dt}\right]\frac{d}{dt}\delta(t-\tau_F). \quad (20)$$

We may apply the temporal derivatives to the excitation or electromechanical coupling responses $h_{\text{pulse}}(t) \equiv h_y(t) * h_y(t) * v(t)$. In this way, the time delay for the system impulse response is τ_F:

$$h(\mathbf{x},t) = p(\mathbf{x},t) * \delta(t-\tau_F(\mathbf{x})) \quad (21)$$

where * is a temporal convolution and

$$p(\mathbf{x},t) = -\frac{\sigma_3^2}{2}\left(\frac{1}{x_1}\right)^2 \frac{1}{\left(\frac{1}{F}-\frac{1}{x_1}\right)^2} \exp -\frac{1}{\sigma_2^2}\frac{F^2}{(F-x_1)^2}x_2^2 \times \left[\frac{1}{\sigma_2^2} - \frac{1}{c}\left(\frac{1}{F}-\frac{1}{x_1}\right)\frac{d}{dt}\right]\frac{d}{dt}h_{\text{pulse}}(t). \quad (22)$$

This time-delay factor can help us reduce the spatial matched filtering operation for image reconstruction to a delay and sum procedure.

C. Spatiotemporal filtering to recover spatial resolution

While spatial bandwidth is a measure of the spatial resolution encoded in a point-spread function, spatiotemporal filtering is required to recover this resolution in unfocused regions of the beam. By time-reversing the point-spread function at a given depth and convolving it with the fixed focus beamformed rf data it is possible to improve lateral spatial resolution, as discussed in previous work, and illustrated in the experimental section of this article. A similar effect can be produced by delay and sum postprocessing.

D. Retrospective delay-and-sum dynamic focusing

Noting that the impulse response of a Gaussian apodized focused aperture can be written as Eq. (21) the spatiotemporal matched filtering procedure involves as its principle operation, convolution with the delta function $\delta(t-\tau_F(x))$, which motivates the delay-and sum reconstruction

$$y(x_2,t|x_1) = \int g(x_2 - x_2', t - \tau_F(x_1, x_2 - x_2')|x_1)dx_2'. \quad (23)$$

The above-presented delay-and-sum procedure can be extended to discrete scan lines $g_n(t)$ and shift-varying dynamic focusing by considering that $x_1 = ct/2$ in expression (19) for τ_F, and ignoring the linear propagation term $2x_1/c$. The mth reconstructed scan line as a function of time is then given as

$$y_m(t) = \sum_n w_n(t) g_{m-n}\left(t + \frac{1}{ct/2 - F}\frac{\Delta x_n^2}{c}\right), \quad (24)$$

where Δx_n is the distance from the center of the walking subaperture to the nth array element, and $w_n(t)$ is a time-dependent aperture weighting function. The aperture should shrink the closer one gets to the focal zone, especially when $k|x_1 - F|$ is not much larger than $(F/\sigma_2)(x_1/\sigma_2)$, as discussed earlier.

E. The virtual source, virtual detector interpretation

The delay function can be derived from simple geometric considerations by understanding that the transmit focal points act as an array of virtual sources. Similarly, the receive focal points act as arrays of virtual detectors. In the fixed focus paradigm, the virtual sources and virtual detectors are spatially identical. Time delays $2x_1/c - (1/x_1 - F) \times (\Delta x_n^2/c)$ represent a Taylor expansion in Δx_n to the hypotenuse $2\sqrt{(\Delta x_n - F)^2 - \Delta x_1^2}/c$ of the triangle whose vertices are the walking subaperture center, field point, and nth virtual element a distance d_n from the subaperture center. Equation (24) thus may be interpreted as a process of applying dynamic time delays to the pulse-echo signals of the virtual array elements to dynamically focus along the desired scan lines. This interpretation helps us consider more general scanning and beamsteering geometries.

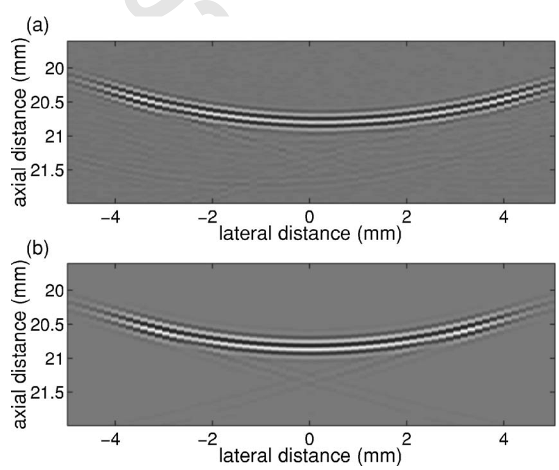

FIG. 1. (a) Measured nearfield psf and (b) simulated psf. We used a VF10-5 array transducer with the following parameters: F-number of 2.1, transmit focus of 4 cm, receive focal distance at 3.9 cm, elevation focus approximately 2 cm, and 6.67 MHz excitation frequency. The array had 192 elements of dimension 0.2×5 mm with 0.02 mm kerf.

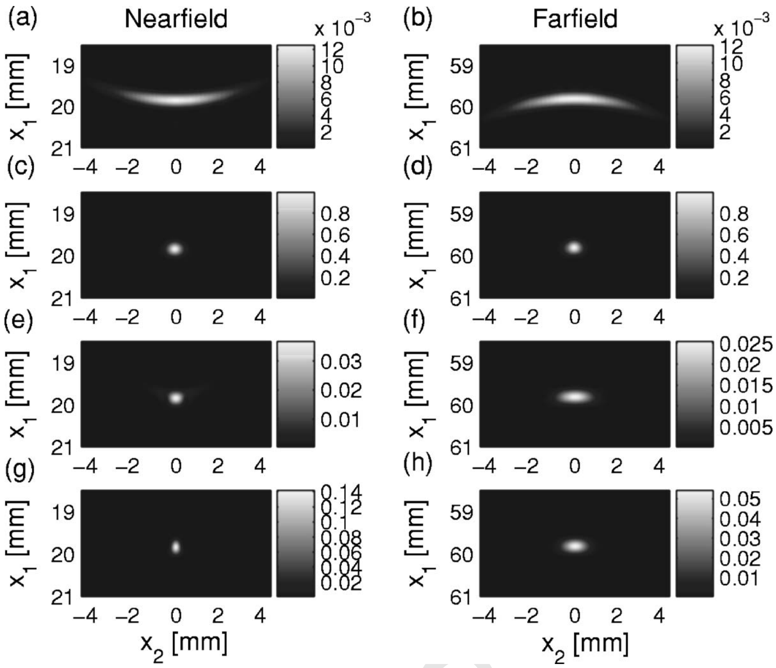

FIG. 2. Comparison of psfs: (a) and (b) Near- and farfield psf due to a Gaussian-apodized (σ=6.7 mm) subaperture truncated at width 2 cm, and with a 4 cm transmit-receive focus. (c) and (d) psf due to retrospective dynamic focusing of the psfs in (a) and (b). (e) and (f) psfs due to dynamic receive focusing with 4 cm transmit focus and same transmit aperture. (g) Nearfield psf due to focusing at 20 mm depth on transmit and receive using the above-mentioned aperture. (h) Farfield psfs due to focusing at 6 cm on transmit and receive using the above-mentioned aperture.

III. SIMULATIONS AND EXPERIMENTS

We use simulations and experiments to test some of our ideas. For experiments, we used a programmable Siemens Sonoline Antares ultrasound scanner. This scanner possesses a commercially available ultrasound research interface (URI) that allows us to control acquisition parameters not accessible in clinical mode, and to save beamformed rf to files for offline analysis. A library of MATLAB functions (offline processing tool or OPT) for reading and processing the data was available to us to assist in our analysis.

A. Nearfield point-spread functions: Experimental validation of simulations

We use FIELD II to simulate psfs to compare with measured psfs from the Antares. This gives us confidence that our simulations are realistic, and allows us the flexibility to try more settings than are allowable with the current URI. To measure the nearfield psf of a fixed-focus beam on the Antares, we used the URI to turn off dynamic receive, aperture growth, and receive apodization functions. We set the receive F-number to 2.1, the transmit focus at 4 cm, and the receive focus at 3.9 cm (the URI allows only several discrete choices for these parameters). To image psfs we simply acquired rf data from sparse dust particles in de-gassed water. The measured and corresponding simulated psf are shown in Fig. 1. The curved wave front of the simulated psf is similar to the measurement.

B. Gaussian-apodized psfs

Having established the accuracy of the simulations in modeling our ultrasound system, we now simulate Gaussian-apodized beams to validate some of the theoretical predictions, and to test the performance of the reconstruction algorithm. Figure 2 shows Gaussian-apodized near- and farfield point-spread functions, including retrospectively focused psf results in Figs. 2(c) and 2(d). The retrospectively filtered psfs have approximately the same lateral spatial resolution as the focal region psf, as shown in Fig. 3 and predicted by Eq. (13). This is also seen in Fig. 4, which shows that the lateral bandwidth is approximately constant through the near- and farfield, and that retrospective dynamic focusing is able to sustain focal-zone lateral spatial resolution through the near- and farfield regions. In the farfield, the spatial resolution attainable with retrospective focusing is finer than that attain-

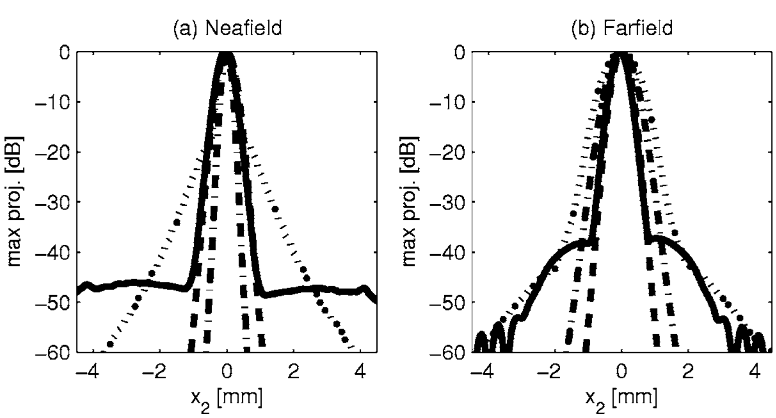

FIG. 3. Normalized cross-range maximum amplitude projections of near (left) and farfield (right) psfs. Solid line: retrospective dynamic focusing; dotted line: the projection of the dynamic receive focusing psf in Figs. 2(e) and 2(f); dashed line: projection of the psf due to a scatterer placed at the 4 cm transmit-receive focus; dot-dashed line: projection of the focused psfs (g) and (h).

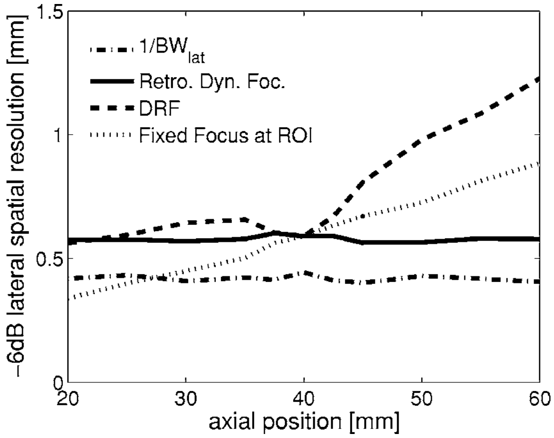

FIG. 4. Full width at half maximum of Gaussian-apodized psfs as a function of axial distance. Solid line: Retrospective dynamic focusing of psfs due to scatterers placed at various depths, using a 2 cm Gaussian-apodized aperture (σ=6.7 mm) focused at 4 cm (transmit and receive); dashed line: resolution curve due to dynamic receive focusing and 4 cm transmit focus; dot-dashed line: the reciprocal of the lateral bandwidth of fixed 4 cm transmit-receive focus psfs as measured by the full width at half maximum of the two-dimensional power spectral density at the axial center frequency; dotted line: the −6 dB beamwidth of a transducer with fixed focus at the plotted axial depth (i.e., focused in the region of interest).

able with dynamic receive focusing and even finer than that attainable when one focuses (transmit and receive) at the region of interest. This means that for a given aperture size, by focusing before rather than at the farfield region, spatial resolution a few aperture lengths away from the transducer can be retrospectively focused with a spatial resolution equivalent to a low *F*# psf. This conclusion may have important implications for applications with limited aperture. Although sidelobes due to retrospective dynamic focusing are nonideal, they are lower than dynamic receive focusing within a couple of millimeters of the mainlobe, and sufficiently low beyond this. The retrospective focusing method further offers enhanced signal-to-noise compared to dynamic receive focusing as evidenced by the grayscale magnitudes in Fig. 2, where each column of psfs is normalized by the maximum of the retrospective focusing image.

C. Comparison with dynamic receive focusing: Unapodized apertures

Here we consider unapodized apertures. We use computer simulations since analytic tractability is more challenging for this case. Figures 5 and 6 show that in the nearfield, the retrospective dynamic focusing method shows comparable spatial resolution to focusing at the region of interest (for a fixed aperture size). This is slightly counterintuitive since Eq. (13) predicted that the spatial bandwidth for a 2 cm transmit focus should be greater than that for a 4 cm transmit focus for a fixed aperture. Computations in Fig. 7 show that the prediction of constant lateral bandwidth with axial depth must be rethought for non-Gaussian apodizations. In fact, it appears that the lateral bandwidth at the 4 cm focus is minimum across the axial range. This roughly explains the retrospective dynamic focusing curve in Fig. 7. In the farfield regions, retrospective dynamic focusing is seen to offer substantial spatial resolution and sidelobe improvements over dynamic receive focusing. Again, similar to the Gaussian apodization case, we see that by focusing before rather than at the farfield region, spatial resolution a few aperture lengths away from the transducer can be retrospectively focused with a spatial resolution equivalent to a low *F*# psf. The retrospective focusing method again offers enhanced signal-to-noise compared to dynamic receive focusing (and even focused imaging).

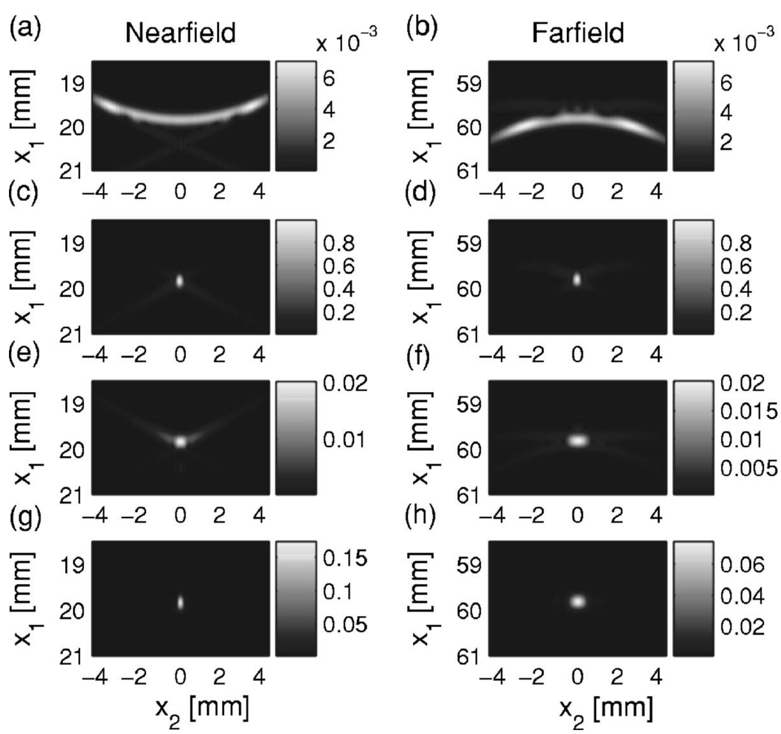

FIG. 5. Comparison of psfs: (a) and (b) Near- and farfield psf due to an unapodized 2 cm walking subaperture, and with a 4 cm transmit-receive focus. (c) and (d) psf due to retrospective dynamic focusing of the psfs in (a) and (b). (e) and (f) psfs due to dynamic receive focusing with 4 cm transmit focus and same transmit aperture. (g) Nearfield psf due to focusing at 20 mm depth on transmit and receive using the above-mentioned aperture. (h) Farfield psfs due to focusing at 6 cm on transmit and receive using the above-mentioned aperture.

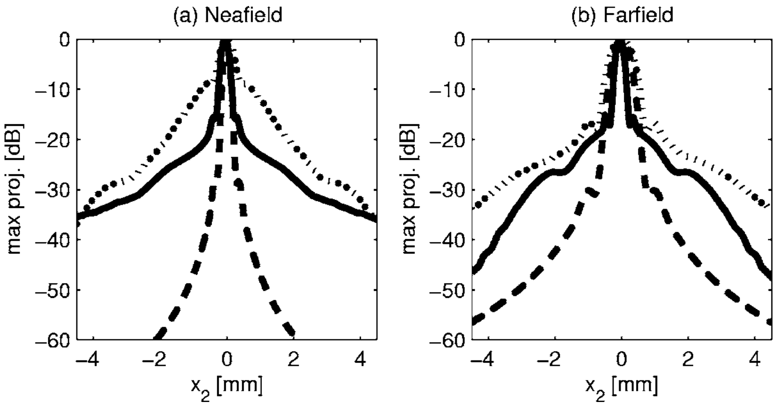

FIG. 6. Normalized cross-range maximum amplitude projections of near (left) and farfield (right) psfs. Solid line: retrospective dynamic focusing; dotted line: the projection of the dynamic receive focusing psf in Figs. 5(e) and 5(f); dashed line: projection of the psf due to a scatterer placed at the 4 cm transmit-receive focus; dot-dashed line: projection of the focused psfs (g) and (h).

D. Phantom experiments

The Siemens Antares was used for phantom experiments. Retrospectively focused images of an anechoic inclusion in a scattering phantom is compared to the image obtained using dynamic receive focusing in the nearfield of an $F/2.1$ linear array transmitting 6.67 MHz broadband pulses in Fig. 8. Improvements in resolution and SNR are apparent visually from the image and from contrast (C) and contrast-to-noise (CNR) estimates in Table I. Here contrast is defined as

$$C = \frac{\mu_i - \mu_b}{\mu_b}, \tag{25}$$

where μ_i and μ_b are the mean envelope-detected signal levels in the inclusion and in the background, respectively. Contrast-to-noise is defined as

$$\mathrm{CNR} = \frac{|\mu_i - \mu_b|}{\sqrt{\frac{1}{2}(\sigma_i^2 + \sigma_b^2)}}, \tag{26}$$

where σ_i and σ_b are the standard deviations of the envelope-detected signal in the inclusion and in the background, respectively. Both lesions were imaged in the nearfield at a depth of 2 cm, and in both cases the transmit focus was set at 4 cm. The F-number in (a) was 2.1. The experimental results are consistent with predictions of improved spatial resolution discussed earlier.

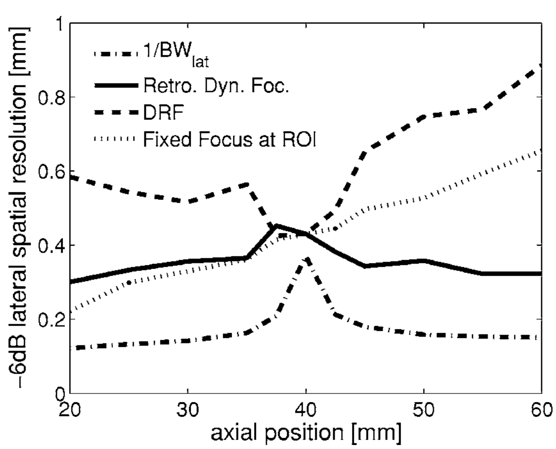

FIG. 7. Full width at half maximum of unapodized psfs as a function of axial distance. Solid line: Retrospective dynamic focusing of psfs due to scatterers placed at various depths, using a 2 cm unapodized aperture focused at 4 cm (transmit and receive); dashed line: resolution curve due to dynamic receive focusing and 4 cm transmit focus; dot-dashed line: the reciprocal of the lateral bandwidth of fixed 4 cm transmit-receive focus psfs as measured by the full width at half maximum of the two-dimensional power spectral density at the axial center frequency; Dotted line: the −6 dB beamwidth of a transducer with fixed focus at the plotted axial depth (i.e., focused in the region of interest).

IV. DISCUSSION

One practical motivation behind fixed focusing rather than dynamic-receive focusing is that front-end ultrasound system complexity is greatly reduced when no dynamic beamforming circuit is required.

One possible architecture could use an analog switch array to route incoming channel data through fixed-delay analog delay lines followed by channel summation. This would eliminate tapped delay lines in analog dynamic-receive beamformers, which have stringent demands on tap intervals that are difficult to obtain over long delays. It also eliminates multiple analog-to-digital converters and fast

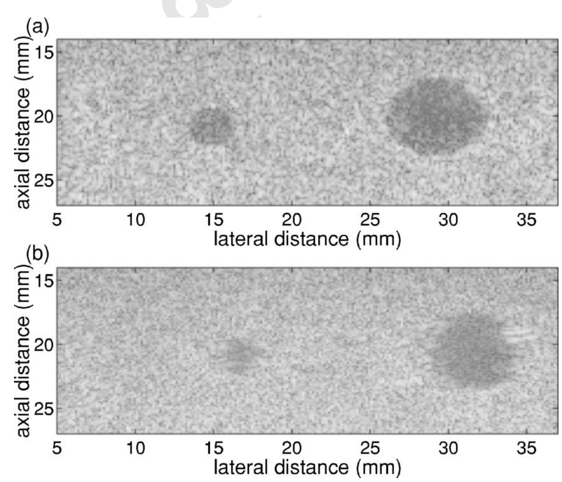

FIG. 8. Anechoic lesion phantom: (a) Nearfield retrospectively focused image, $F\# = 2.1$. (b) Dynamic receive focusing image. In both images the transmit focus is at 4 cm.

TABLE I. Anechoic lesions: Comparison of retrospectively focused nearfield imaging with dynamic receive focusing.

Method	C	CNR
	Large lesion	
Retro. Foc.	−0.75	1.5
DRF	−0.61	1.0
	Small Lesion	
Retro. Foc.	−0.71	1.4
DRF	−0.45	0.8

FIFO memory prevalent in digital systems, thus reducing cost and complexity. The option of switching between a few focal zones or using multiple focal zones in a scan could further enhance flexibility for image quality.

Another important application may be in high-frequency ultrasound systems using mechanically scanned high-numerical aperture single element transducers. The developments here may prove important for improving image quality away from the focal zone.

Potential artifacts and promising solutions. A known issue with spatiotemporal filtering is that sidelobe levels are higher than desired. This article's purpose is to provide a fundamental perspective imaging with unfocused regions of focused beams, hence we do not explicitly deal with sidelobe reduction strategies. Apodization methods may prove advantageous as may filtering channel data before beamforming, as discussed by Kim *et al.*[21] This may be a topic of future research.

Motion within the scan duration could produce significant artifacts using unfocused imaging techniques. Some groups, however, have successfully implemented related synthetic aperture techniques *in vivo* at very high frame rates.[22] If scan times are fast enough, motion artifacts may be minimal.

Phase aberrations could be another source of artifacts. Aberrations due to differences in the speed of sound in tissue or due to refractive tissue interfaces could shift energy away from the expected wave fronts. This, however, is also a problem for conventional focused imaging using DRF methods. Moreover, deaberration strategies or filtering techniques may prove useful. Understanding these concepts better and applying them to *in vivo* imaging should be a topic of future work. A rigorous investigation is not within the scope of this article.

V. CONCLUSIONS

By studying the spatial bandwidth in Gaussian apodized point-spread functions, we conclude that spatial resolution encoded in curved wave fronts remains approximately constant throughout the nearfield, focal, and farfield zones. A retrospective dynamic focusing approach successfully recovers this resolution, and may provide a solution to the problem of loss of spatial resolution away from the transmit focus in present state-of-the art dynamic receive focusing array systems.

ACKNOWLEDGMENT

We acknowledge partial support from NIH R01 CA 082497.

[1]R. J. Zemp, M. D. Parry, C. K. Abbey, and M. F. Insana, "Detection performance theory for ultrasound imaging systems," IEEE Trans. Med. Imaging **24**, 300–310 (2005).
[2]C. K. Abbey, R. J. Zemp, and M. F. Insana, "Pre-envelope deconvolution for increased lesion detection efficiency in ultrasonic imaging," Proc. SPIE **5034** (2003).
[3]T. S. F. Lingvall and T. Olofsson, "Synthetic aperture imaging using sources with finite aperture-deconvolution of the spatial impulse response," J. Acoust. Soc. Am. **114**, 225–234 (2003).
[4]K. Ranganathan and W. F. Walker, "A novel beamformer design method for medical ultrasound. I. Theory," IEEE Trans. Ultrason. Ferroelectr. Freq. Control **50**, 15–24 (2003).
[5]J. Jensen, J. Mathorne, T. Gravesen, and B. Stage, "Deconvolution of *in-vivo* ultrasound B-mode images," Ultrason. Imaging **15** (1993).
[6]C. K. Abbey, R. J. Zemp, J. Liu, K. K. Lindfors, and M. F. Insana, "Observer efficiency in discrimination tasks simulating malignant and benign breast lesions with ultrasound," IEEE Trans. Med. Imaging **25**, 198–209 (2006).
[7]B. Haider, P. Lewin, and K. E. Thomenius, "Pulse elongation and deconvolution filtering for medical ultrasonic imaging," IEEE Trans. Ultrason. Ferroelectr. Freq. Control **45** (1998).
[8]J. A. Jensen and P. Gori, "Spatial filters for focusing ultrasound images," *Proceedings of the IEEE Ultrasonics Symposium*, 2001, pp. 1507–1511.
[9]M. Fink, "Time reversal of ultrasonic fields. I. Basic principles," **39**, 555–566 (1992).
[10]G. S. Kino, *Acoustic Waves: Devices, Imaging and Analog Signal Processing* .
[11]S. Freeman, P. C. Li, and M. O'Donnell, "Retrospective dynamic transmit focusing," Ultrason. Imaging **17**, 173–196 (1995).
[12]G.-S. Jeng and S.-W. Huang, "SNR-dependent filter design for improving depth of field using modified least squares," *Proceedings of the IEEE Ultrasonics Symposium*, 2003, pp. 1235–1238.
[13]M. L. Li and P. C. Li, "Filter based synthetic transmit and receive focusing," Ultrason. Imaging **23**, 73–89 (2001).
[14]S. Nikolov and J. A. Jensen, "Virtual ultrasound sources in high-resolution ultrasound imaging," Proc. SPIE **3**, 395–405 (2002).
[15]C. Passman and H. Ermert, "A 100 MHz ultrasound imaging system for dermatologic and ophthalmologic diagnostics," IEEE Trans. Ultrason. Ferroelectr. Freq. Control **43**, 545–552 (1996).
[16]C. Frazier and W. O'Brien, "Synthetic aperture techniques with a virtual source element," IEEE Trans. Ultrason. Ferroelectr. Freq. Control **45**, 196–207 (1998).
[17]P. R. Stepanishen, "Acoustic transients from planar axisymmetric vibrators using the impulse response approach," J. Acoust. Soc. Am. **70**, 1176–1181 (1981).
[18]J. W. Goodman, *Introduction to Fourier Optics*, 2nd ed. (McGraw-Hill, New York) (1996).
[19]R. Zemp, "Detection theory in ultrasonic imaging," Dissertation, University of California, Davis, (2004).
[20]R. J. Zemp and M. F. Insana, "Spatial coding with curved wavefronts," in *Proceedings of the IEEE Ultrasonics Symposium*, 2004.
[21]K. S. Kim, J. Liu, and M. F. Insana, "Efficient array beam forming by spatial filtering for ultrasound B-mode imaging," J. Acoust. Soc. Am. **120**, 852–861 (2006).
[22]J. A. Jensen *et al.*, "Ultrasound research scanner for real-time synthetic aperture data acquisition," IEEE Trans. Ultrason. Ferroelectr. Freq. Control **52**, 881–891 (2005).